ACS Sustainable Chemistry & Engineering

Research Article

pubs.acs.org/journal/ascecg

Preparation of CTAB-Assisted Hexagonal Platelet $Co(OH)_2$/Graphene Hybrid Composite as Efficient Supercapacitor Electrode Material

Debasis Ghosh, Soumen Giri, and Chapal Kumar Das*

Materials Science Centre, Indian Institute of Technology Kharagpur, Kharagpur 721302, India

Supporting Information

ABSTRACT: In this paper, our work deals with the preparation of cetyl trimethylammonium bromide (CTAB)-assisted hexagonal platelet β $Co(OH)_2$ via a simple hydrothermal process and its graphene-based hybrid composite with improved electrochemical properties. The prepared materials were successfully characterized by FTIR, XRD, FESEM, TEM, and TGA analysis. The materials were subjected to electrochemical analysis by a three electrode system in a 6 M KOH electrolyte in terms of a cyclic voltammetry, cyclic charge−discharge, and electrochemical impedance study. The CTAB-assisted $Co(OH)_2$ with hexagonal architecture exhibited the highest specific capacitance of 312 F/g at a 2 mV/s scan rate and 285 F/g at a 2 A/g constant discharge current density. The high utility of pseudocapacitive $Co(OH)_2$ is achieved only in its graphene-based hybrid composite, which responded with specific capacitance of 532 F/g at a 2A/g current density and a 94% specific capacitance retention over 500 charge discharge cycles.

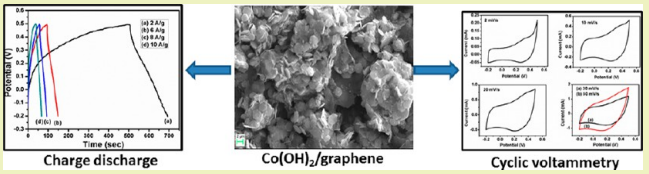

KEYWORDS: *Cobalt hydroxide, Graphene, Specific capacitance, Supercapacitor*

INTRODUCTION

The growing interest with depleting fossil fuels and worldwide concern of the global warming effect is the prior incentive to develop alternative energy sources. Scientists are searching for alternative and pollution free energy resources, typically ultracapacitors or supercapacitors with hybrid properties of conventional batteries and conventional capacitors in terms of high energy density and high power density.[1] The unique properties of supercapacitors also include fast charge−discharge time, high cycle stability, and applications in the various fields of automobile, spaceship, memory backup, military, etc.[2] Supercapacitors can store energy at the electrode−electrolyte interface, which involves the physically opposite charge separation and are typically called electric double-layer capacitors (EDLC). Another way of charge storage in supercapacitors involves the redox reactions occurring in the electrode material; these are known as pseudocapacitors.[3] EDLC is mainly comprised of high surface area carbon materials such as activated carbon, carbon nanotube, graphene, etc., whereas pseudocapacitors cover the wide range of metal oxides or hydroxides, spinal compounds, conductive polymers, etc. RuO_2, MnO_2, ZnO, $Ni(OH)_2$, $NiCo_2O_4$, etc.[4−8] have been extensively investigated as efficient pseudocapacitive materials, eitehr stand alone or within a composite. Apart from these, $Co(OH)_2$ is one of the most interesting pseudocapacitive materials with distinct redox activity and relatively low cost. Theoretically, the specific capacitance of $Co(OH)_2$ can reach as high as 2600 F/g and even more.[9] The surface area and morphology of the electrode materials affect the stored energy to a greater extent. Nanostructured electrode materials with high surface area as well as good porosity offer an extended contact area with the electrolyte as well as the rapid transfer of electrolyte ions, which helps to decrease the equivalent series resistance (ESR).[10,11] Many approaches have been proposed to synthesize $Co(OH)_2$ with different surface morphologies offering specific capacitance. Ji et al. have obtained a specific capacitance of 170 F/g at a discharge current density of 0.5 μA for the printable thin film β $Co(OH)_2$ supercapacitor.[12] Hu et al. have reported specific capacitance of about 416.7 F/g for sheet-like $Co(OH)_2$.[13] Yuan et al. have achieved specific capacitance of 341 F g^{-1} for mesoporous $Co(OH)_2$ at a current density of 5 mA cm^{-2} and 434 F g^{1-} at 1.33 A/g (10 mA cm^{-2}) discharge current density for the flowery $Co(OH)_2$.[14,15] However, the problems with such types of pseudocapacitors are their electrically insulating nature, low working potential, and low cycle stability, which restricts their applications in various fields. A combination of the EDLC property of the carbonaceous materials with the pseudocapacitve redox active materials may help in this respect and is the main focus among the research community in recent years.[16−18] Apart from the pseudocapacitive materials, graphene is a unique carbonaceous material with a 2D array of sp^2 hybridized carbon atoms, offering the highest specific surface area along with high porosity and the highest conductivity among all the carbonaceous materials. Incorporation of these pseudocapacitive materials to graphene has the prospective to take the benefits of both components to achieve greatly improved properties.[19] Therefore, graphene can be treated as an ideal substrate for the growth of functional nanomaterials due to the large specific surface area, and it also makes the materials electrically conductive and electrochemically active to the outside current collectors.[20] Our present work focuses on a

Received: February 22, 2013
Revised: May 23, 2013
Published: June 3, 2013

novel hydrothermal synthesis of a CTAB-assisted $Co(OH)_2$ plate with distinct architecture, along with the facile ex situ growth of the platelet $Co(OH)_2$ on the graphene surface. Experiments show that the high utilization of the $Co(OH)_2$ material can be achieved only in its graphene-based composite with excellent rate capability and increased energy density.

EXPERIMENTAL SECTION

Reagents and Instruments. See S1 of the Supporting Information.

Method. Fifteen milliliters of 0.2 M NH_4OH solution was added drop by drop to 15 mL 0.1 M $CoCl_2$ solution in three different sets with constant stirring for 5 min. During the addition of $CoCl_2$ with NH_4OH, an immediate precipitation started simultaneously. Ten milliliters of CTAB solution with concentration of 0.01 and 0.02 M was added to two of the three sets. Then, the solution mixtures were transferred into three different 50 mL screw-capped test tubes and were placed in a closed wooden box under a 200 W tungsten bulb for 12 h. The resulting materials were collected and centrifuged several times with 1% ethanol−water and dried in an oven maintaining a temperature of 60 °C. For preparation of the hybrid composite, first, 30 mg graphene was well dispersed in 150 mL of water using 0.6 g CTAB by ultrasonication for 30 min. Then, 60 mg of the 0.02 M CTAB-assisted $Co(OH)_2$ was added to the dispersed graphene suspension and further sonicated for 5 min. The whole mixture was stirred with the help of a magnetic stirrer for 5 h at 500 rpm. Then, the suspension was kept unstirred for another 6 h. The constant agitation helps to grow the $Co(OH)_2$ on the graphene surface. The mixture was then centrifuged and dried at 60 °C and collected. We used the ratio of the as-prepared CTAB-assisted $Co(OH)_2$ to graphene quite arbitrarily keeping in mind the high cost of graphene and its efficiency toward increasing the specific capacitance and especially the cycle life of the electrode material. The $Co(OH)_2$ prepared without CTAB was labeled as $Co(OH)_2$, whereas the $Co(OH)_2$ prepared with 0.02 M CTAB was labeled as CT-$Co(OH)_2$. The graphene-based hybrid composite of the 0.02 M CTAB-assisted $Co(OH)_2$ was labeled as CT-$Co(OH)_2$/graphene.

RESULTS AND DISCUSSION

The XRD patterns of $Co(OH)_2$, CT-$Co(OH)_2$, and CT-$Co(OH)_2$/graphene composite are shown in Figure 1. The

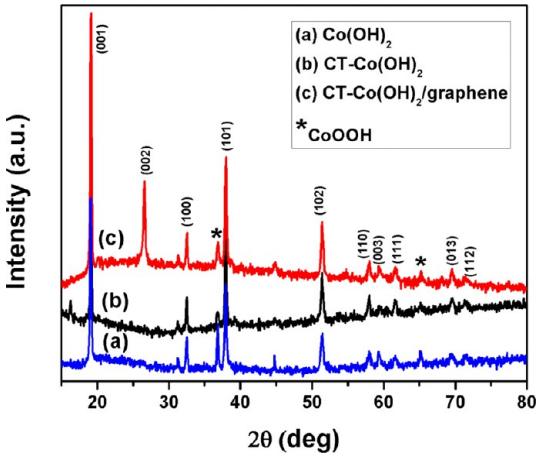

Figure 1. XRD patterns of $Co(OH)_2$, CT-$Co(OH)_2$, and CT-$Co(OH)_2$/graphene composite.

XRD pattern of the $Co(OH)_2$ with or without CTAB exhibits similar diffraction peaks. The diffraction peaks at 2θ values for 19.05°, 32.44°, 37.86°, 51.3°, 57.9°, 59.5°, 61.49°, 69.48°, and 71.53° demonstrate crystalline planes (001), (100), (101), (102), (110), (003), (111), (013), and (112) of β $Co(OH)_2$, respectively. The peaks are in well agreement with JCPDS file card no. 01-073-6993. For the CT-$Co(OH)_2$/graphene composite, all the peaks of the $Co(OH)_2$ were present with an additional crystallinity induced at 2θ of 26.45° corresponding to the (002) plane of exfoliated graphene.[21] The other two peaks at 36.78° and 65.28° can be attributed as some impure phase corresponding to CoOOH formation. All the XRD data reveals the brucite-like phase of β $Co(OH)_2$.

The FTIR plots of the $Co(OH)_2$, CT-$Co(OH)_2$, and the CT-$Co(OH)_2$/graphene composite are shown in Figure 2. The FTIR

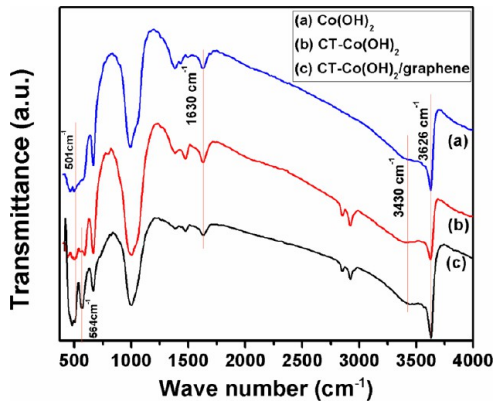

Figure 2. FTIR of $Co(OH)_2$, CT-$Co(OH)_2$, and CT-$Co(OH)_2$/graphene composite.

spectra of all three materials exhibited a broad band centered at 3430 cm^{-1} indicating the O−H stretching vibration of the interlayer water molecule and the O−H group H atom bonded to a water molecule.[22] The sharp peak at 3626 cm^{-1} can be assigned to the O−H stretching vibration of non-H bonded Co−OH group.[23] The low frequency peaks in the range 430−590 cm^{-1} are assigned to the Co−O stretching and Co−OH bending vibrations.[24] Another sharp peak at 1630 cm^{-1} can be attributed to the bending vibration of the absorbed interlayer water molecule. The FTIR plots (Figure 2a,b) confirm the successful formation of $Co(OH)_2$ and its presence in the CT-$Co(OH)_2$/graphene composite (Figure 2c).

Morphological Analysis. CTAB as a cationic surfactant plays an important role in controlling the formation of micro and nano architectures under the template effect. The growth of the certain architecture is associated with the selective interaction of the organic surfactants on certain crystallographic facets to stimulate the crystal growth.[25,26] For better understanding the template effect, we prepared the $Co(OH)_2$ with and without using the surfactant and varied the surfactant concentration. The FESEM images of the $Co(OH)_2$ with or without CTAB and the CT-$Co(OH)_2$/graphene composite are shown in Figure 3. $Co(OH)_2$ prepared without CTAB (Figure 3a) exhibits nanopod morphology with no uniform dimension. Figure 3(b) and (c) represent the FESEM micrographs of the prepared $Co(OH)_2$ using CTAB with concentrations of 0.01 and 0.02 M, respectively. CTAB with concentration of 0.01 M assists $Co(OH)_2$ to gain a hexagonal platelet morphology, whereas with higher CTAB concentration of 0.02 M, more regular and distinct hexagonal $Co(OH)_2$ plates can be observed with an average thickness of 284 nm. In Figure 3(d), a noticeable distribution of a large number of hexagonal plates of CT-$Co(OH)_2$ with uniform dimensions on the graphene surface clearly indicates some chemical as well as electrostatic interactions between the couple. The quite uniform distribution of the CT-$Co(OH)_2$ particle over the graphene surface with

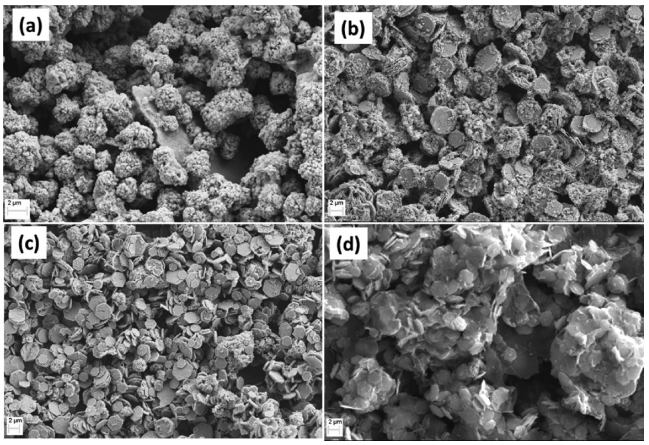

Figure 3. FESEM micrographs of prepared $Co(OH)_2$: (a) without using CTAB, (b) using 0.01 M CTAB, (c) using 0.02 M CTAB, and (d) the CT-$Co(OH)_2$/graphene composite.

hardly any bare graphene sheet and the least agglomeration indicates the fruitful use of CT-$Co(OH)_2$ to graphene in a weight ratio of 2:1, which could have better synergistic interaction. The TEM images of the hexagonal platelet CT-$Co(OH)_2$ and CT-$Co(OH)_2$/graphene composite are shown in Figure 4(a) and (b), respectively. The TEM image clearly demonstrate the growth of CT-$Co(OH)_2$ hexagonal plates on the graphene surface. In Figure 4(c), the selected area diffraction pattern of the CT-$Co(OH)_2$ reveals its single crystalline nature. The lattice fringes in Figure 4(d) are separated by a distance of about 0.46 nm representing the (001) crystalline plane. In the XRD pattern, the strongest peak obtained was also (001). Thus both of these confirm that the CT-$Co(OH)_2$ hexagonal plate grows mainly along the (001) direction. On the basis of the morphology of the prepared $Co(OH)_2$, a reaction scheme is illustrated in Scheme 1, and the reaction scheme of the formation of CT-$Co(OH)_2$/graphene is illustrated in Scheme 2.

Thermogravimetric Analysis. The TGA curves of $Co(OH)_2$ and CT-$Co(OH)_2$ and its graphene-based composite are represented in Figure 5 within the temperature range of 30−800 °C. The as-prepared $Co(OH)_2$ and CT-$Co(OH)_2$ showed weight loss of 23.06% and 23.77%, respectively, whereas at the end, the CT-$Co(OH)_2$/graphene composite ended with only 20.6% weight loss. Although the overall thermal stability of the CT-$Co(OH)_2$ was lower than that of $Co(OH)_2$, the former exhibited better thermal behavior up to 680 °C. The weight loss associated with particular temperature ranges are stated below. The weight loss in the region of 50−150 °C is associated with the weight loss due to the absorbed water. The second stage of weight loss up to 260 °C is associated with the interlayered water evaporation. The major weight loss occurs [12.63% for $Co(OH)_2$ and 13.95% for CT-$Co(OH)_2$] within the temperature range of 170−330 °C, which is related to the loss of the −OH group of $Co(OH)_2$ and also accompanied by the conversion to spinal Co_3O_4.[27] The CT-$Co(OH)_2$/graphene composite also exhibited similar nature of thermal degradation but was associated with an overall 3.17% less weight loss than CT-$Co(OH)_2$.

Electrochemical Properties. The electrochemical characterizations of the $Co(OH)_2$, CT-$Co(OH)_2$, and CT-$Co(OH)_2$/graphene composite were carried out in terms of a cyclic voltammetry (CV), galvanostatic charge discharge (GCD), and electrochemical impedance spectroscopy (EIS) study. A working

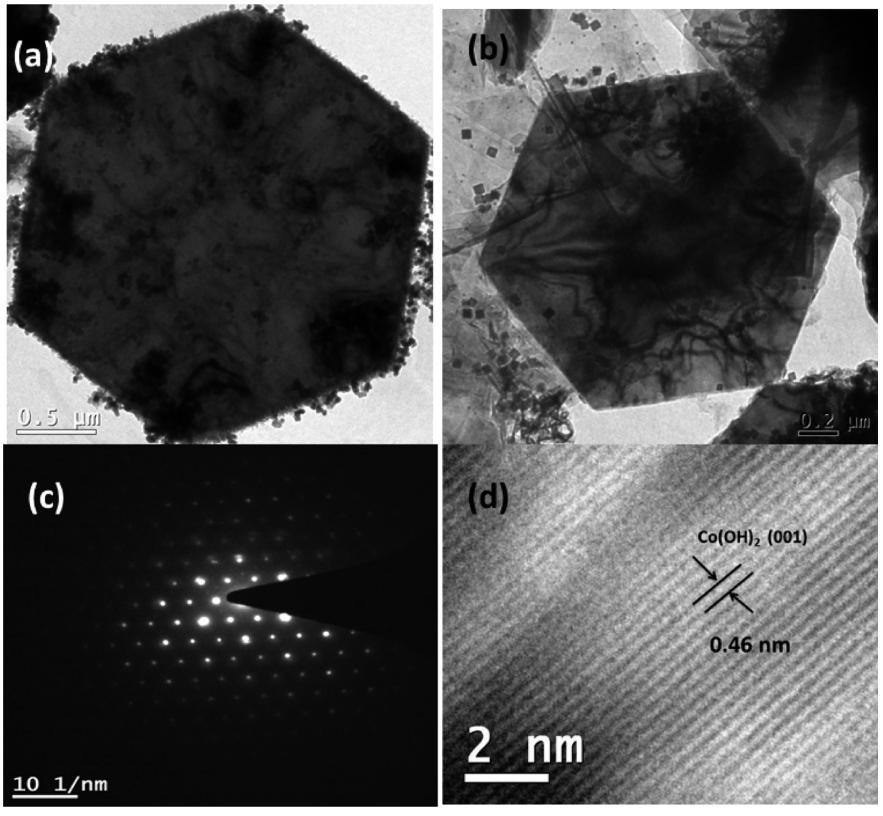

Figure 4. TEM micrographs of (a) CT-$Co(OH)_2$, (b) CT-$Co(OH)_2$/graphene, (c) SAED pattern of CT-$Co(OH)_2$, and (d) lattice fringes of CT-$Co(OH)_2$.

dx.doi.org/10.1021/sc400055z | ACS Sustainable Chem. Eng. 2013, 1, 1135−1142

Scheme 1. Reaction Scheme of Formation of $Co(OH)_2$ and Effect of CTAB on Its Morphology

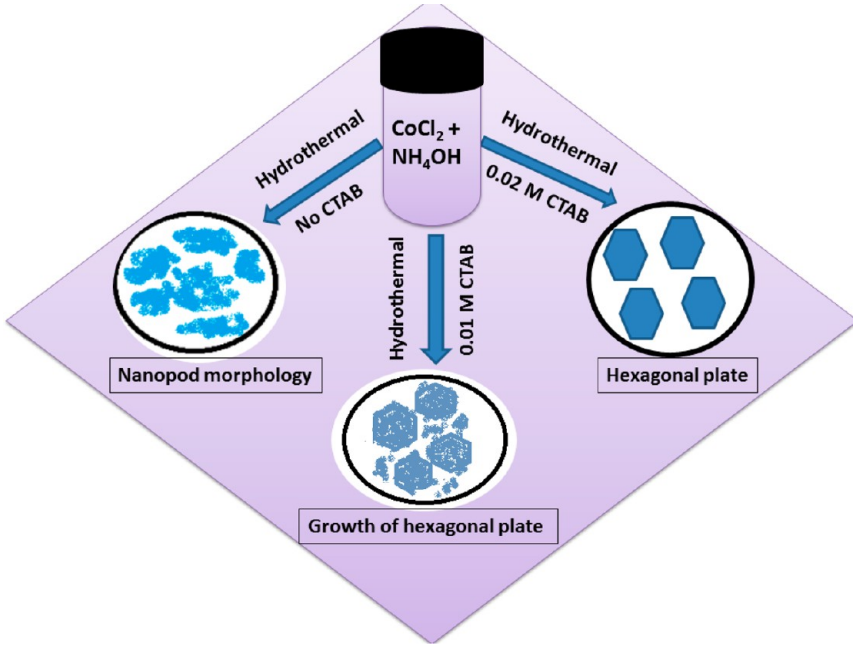

Scheme 2. Reaction Scheme of Formation of CT-$Co(OH)_2$/Graphene Composite

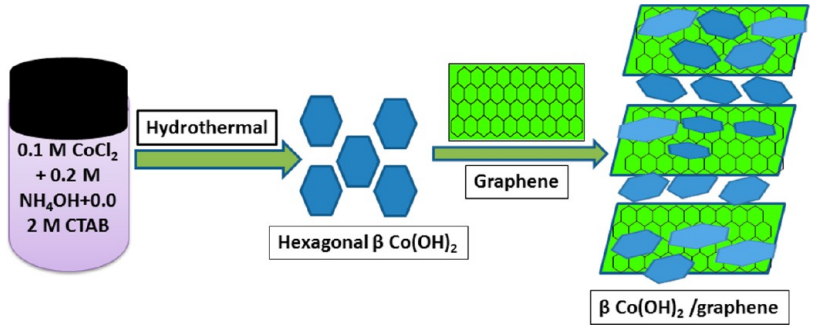

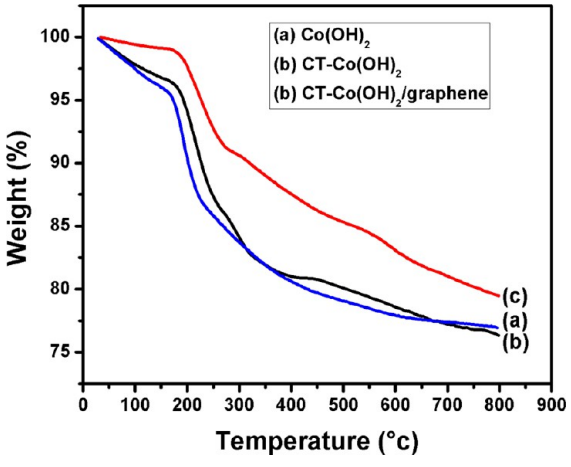

Figure 5. TGA plot of $Co(OH)_2$, CT-$Co(OH)_2$, and CT-$Co(OH)_2$/graphene composite within the temperature range of 30−800 °C.

potential of 0−0.4 V was chosen for $Co(OH)_2$ and CT-$Co(OH)_2$ in a 6 M KOH electrolyte, within which the materials behaved the best. For the CT-$Co(OH)_2$/graphene composite, the best electrochemical behavior was obtained within the potential range from −0.2 to 0.5 V. The specific capacitance was calculated from the CV plots by using the following equation

Specific Capacitance

$$C_S = \frac{\int_{V1}^{V2} i(V)\mathrm{d}V}{(V_2 - V_1)\nu m} \quad (1)$$

where the numerator indicates the charge under the CV curve, i is the instantaneous current at any voltage. V_2 and V_1 are the upper and lower voltage limit, ν is the potential sweep rate, and m is the electrode mass. Figure 6 (I), (II), and (III) represent the CV plots of $Co(OH)_2$, CT-$Co(OH)_2$, and CT-$Co(OH)_2$/graphene hybrid composite at various scan rates of 2 mV/s, 10 mV/s, 20 mV/s, 30 mV/s, and 50 mV/s. The highest specific capacitance exhibited by the $Co(OH)_2$ and CT-$Co(OH)_2$ at a 2 mV/s scan rate was 305 and 316 F/g, respectively, with quite comparable CV plots. The direct growth of the platelet CT-$Co(OH)_2$ on the graphene surface ensures better synergistic interaction with the high surface area graphene, which could enhance the utilization and specific capacitance of the hybrid composite. The specific capacitance was enhanced up to 572 F/g at a 2 mV/s scan rate for the CT-$Co(OH)_2$/graphene composite, high enough compared to that of CT-$Co(OH)_2$ alone. To evaluate rate capability, the CV test was also performed at higher scan rates of 10 mV/s, 20

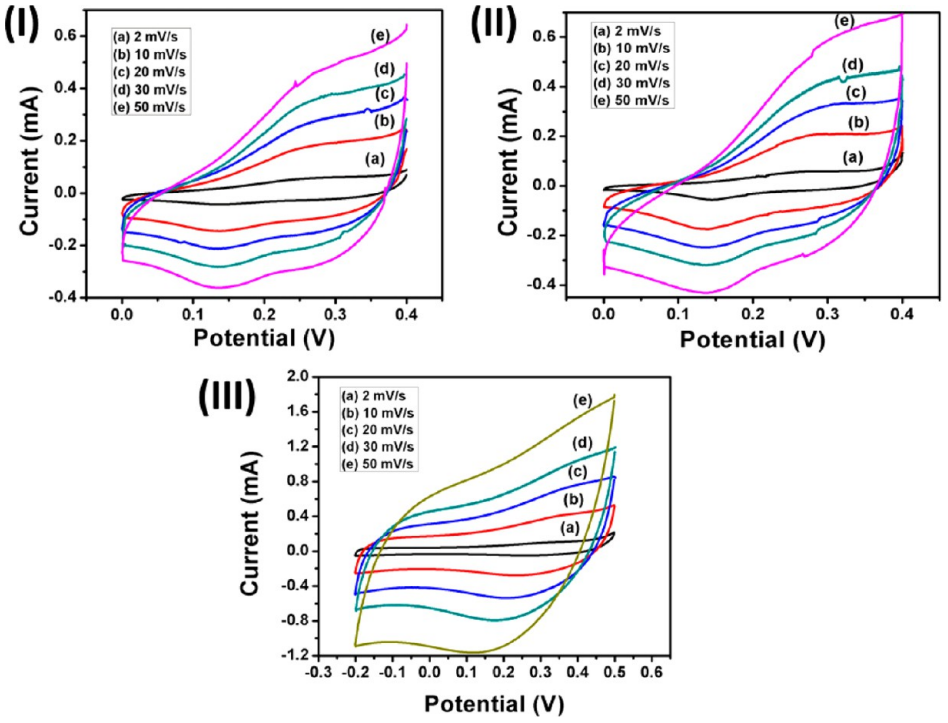

Figure 6. CV plots of (I) $Co(OH)_2$, (II) CT-$Co(OH)_2$, and (III) CT-$Co(OH)_2$/graphene composite at various scan rates of 2 mV/s, 10 mV/s, 20 mV/s, 30 mV/s, and 50 mV/s.

Table 1. Variation of Specific Capacitance with Scan Rates for $Co(OH)_2$, CT-$Co(OH)_2$, and CT-$Co(OH)_2$/Graphene Composite

scan rate	2 mV/s (F/g)	10 mV/s (F/g)	20 mV/s (F/g)	30 mV/s (F/g)	50 mV/s (F/g)
sp. cap. of $Co(OH)_2$	305	218	170	142	127
sp. cap. of CT-$Co(OH)_2$	317	223	173	152	140
sp. cap. of CT-$Co(OH)_2$/graphene	572	482	442	421	392

mV/s, 30 mV/s, and 50 mV/s for all the $Co(OH)_2$, CT-$Co(OH)_2$, and CT-$Co(OH)_2$/graphene composites. The various specific capacitances obtained at different scan rates are shown in Table. 1. At high scan rates, the contribution of the pseudocapacitance to the total capacitance restricts due to the slow faradaic process, which results in a decreased specific capacitance. For the $Co(OH)_2$, CT-$Co(OH)_2$, and CT-$Co(OH)_2$/graphene composite, the specific capacitance obtained at a high scan rate of 50 mV/s was 41%, 44%, and 69%, respectively, to that of specific capacitance obtained at a 2 mV/s scan rate (where a quite high contribution of the pseudocapacitance is achieved). At a high scan rate, sufficient ion diffusion cannot take takes place due to the time constant, and only the outer active sites are used for charge storage. The CT-$Co(OH)_2$/graphene composite offers more surface active sites for charge storage even at a high scan rate resulting in a good rate capability. All the materials exhibited a pair of redox peaks in the CV plots associated with the following redox reaction occurring within the alkali electrolyte

$$Co(OH)_2 + OH^- = CoOOH + H_2O + e^- \text{ and } CoOOH + OH^- = CoO_2 + H_2O + e-$$

The first one is associated with the oxidation peak during the charging process, while the second reaction is associated with the reduction peak during the discharging process. As the scan rate decreases, the peaks become more prominent, signifying the slow faradaic reaction to occur predominantly at low scan rate. It is noteworthy that with the increasing scan rate the cathodic and anodic peaks exhibited a cathodic and anodic shift, which corresponds to the electrode resistance. With the increasing scan rate, the cathodic and anodic current increases linearly indicating a diffusion controlled doping and dedoping process.[28] The deviation from the perfect rectangular shape of the CV plots of all the $Co(OH)_2$, CT-$Co(OH)_2$, and CT-$Co(OH)_2$/graphene composite indicates the significant contribution of pseudocapacitance to the total capacitance.

The performance of the electrode materials were further analyzed with the help of the galvanostatic charge discharge method. From the charge discharge plots, the specific capacitance was calculated from the following equation

Specific Capacitance

$$C = \frac{i \times t}{m \times \Delta v} \quad (2)$$

where, i/m represents constant charging and discharging current density (A/g), t denotes the discharge time (s), and Δv represents the working potential in (V). Figure 7 (I) represents the typical comparative galvanostatic charge discharge (GCD) plots of the $Co(OH)_2$ and CT-$Co(OH)_2$ at 2 A/g constant current density. The discharge plots were quite similar in nature and responded with specific capacitance of a maximum of 276 F/g and 285 F/g, respectively, for $Co(OH)_2$ and CT-$Co(OH)_2$. Figure 7 (II) and (III) represent the GCD plots of the CT-$Co(OH)_2$ and CT-$Co(OH)_2$/graphene composite at various

dx.doi.org/10.1021/sc400055z | ACS Sustainable Chem. Eng. 2013, 1, 1135−1142

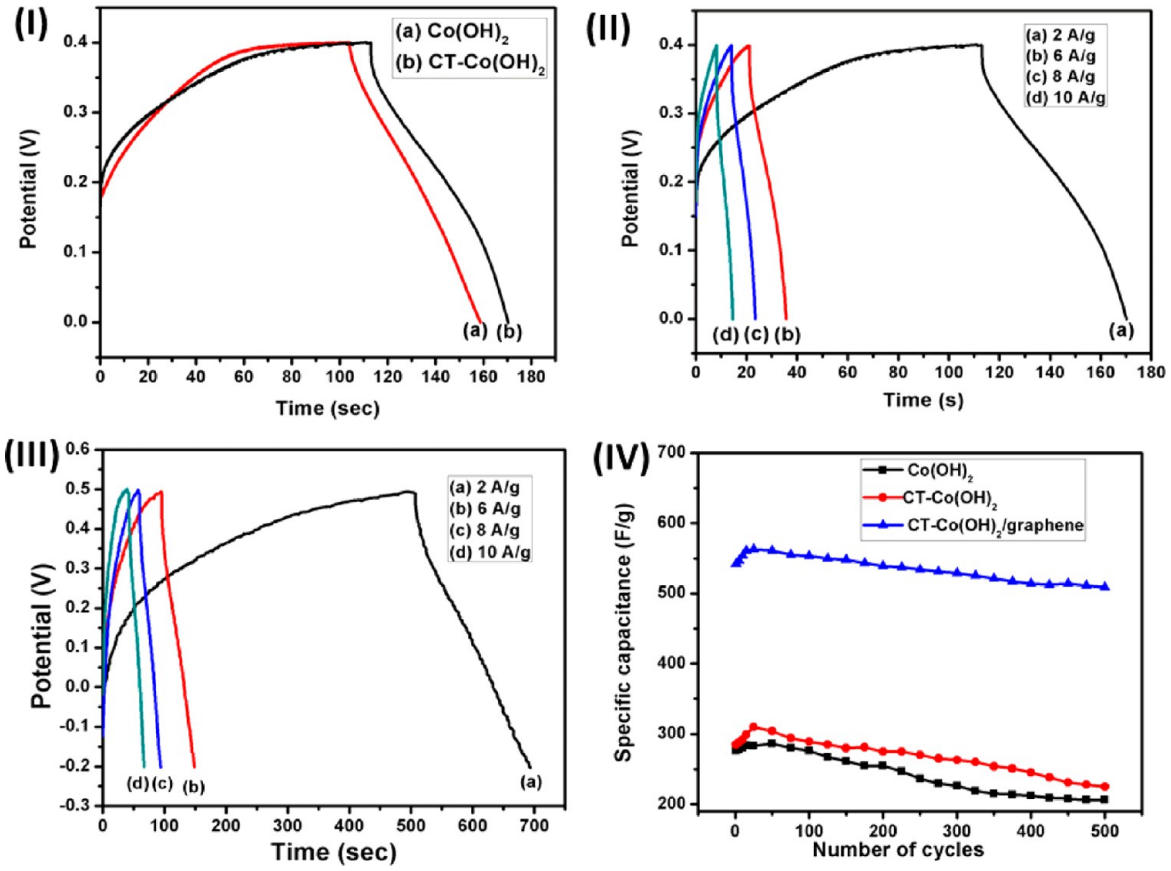

Figure 7. (I) Comparative galvanostatic charge−discharge plots of $Co(OH)_2$ and CT-$Co(OH)_2$ at a constant charge−discharge current density of 2 A/g. GCD plots of (II) CT-$Co(OH)_2$ and (III) CT-$Co(OH)_2$/graphene at different constant current density of 2, 6, 8, and 10 A/g. (IV) Plots of variation of specific capacitance as a function of cycle number of $Co(OH)_2$, CT-$Co(OH)_2$, and CT-$Co(OH)_2$/graphene composite at 2 A/g constant current density.

current density of 2, 6, 8, and 10 A/g. In the case of $Co(OH)_2$ and CT-$Co(OH)_2$, the charge discharge test was carried out within the potential limitation of 0−0.4 V. Going for high working potential resulted in a very low columbic efficiency. The charge discharge test for the $Co(OH)_2$/graphene was carried out within the potential window of −0.2 V to 0.5 V. The large working potential can be attributed to the presence of graphene and the increased synergistic interaction between $Co(OH)_2$ and graphene in aquous alkaline electrolyte. The high utilization of the pseudocapacitive CT-$Co(OH)_2$ was obtained with its graphene-based composite exhibiting maximum specific capacitance of 532 F/g at 2 A/g current density. The various specific capacitances obtained at different current densities are shown in Table 2. On increasing current density, the specific capacitance value exhibits a linear decrease. At high current density, the partial active material has minimum time to respond, resulting in a decreased specific capacitance.[29] For the $Co(OH)_2$/graphene composite, about a 67% specific capacitance retention at high current density of 10 A/g with respect to 2A/g current density is a significance of excellent rate capability. The discharge curves for both the CT-$Co(OH)_2$ and CT-$Co(OH)_2$/graphene composite deviate from perfect linearity indicating the effective contribution of pseudocapacitance to the total capacitance, which is also in agreement with the CV tests results. The charge discharge test was continued to 500 cycles for all the materials at 2 A/g current density, and the variation of specific capacitance with cycle number is represented in Figure 7 (IV). Although $Co(OH)_2$ and CT-$Co(OH)_2$ exhibited comparable specific capacitance, the latter displayed a considerably higher cycle stability of 79% compared to that of the $Co(OH)_2$ with only 75% cyclic stability. About 94% of the initial specific capacitance retention can be observed for the CT-$Co(OH)_2$/graphene hybrid composite, high enough compared to that of both $Co(OH)_2$ and CT-$Co(OH)_2$. The excellent cycle stability of the CT-$Co(OH)_2$/graphene composite electrode can be attributed to the presence of flexible graphene. The amount of flexible graphene sheet used enables excellent flexibility of the CT-$Co(OH)_2$/graphene composite to provide sufficient void spaces to buffer the bulk change and reduce the strain associated with the volume variant during the consecutive charge discharge process. It is noteworthy that all the electroactive materials responded with an increase in specific capacitance for the first 30−35 cycles followed by a regular decrease. This indicates that the full utilization of the electrode material can be achieved only after first 30−35 charge−discharge cycles. The energy density and power density of the as-

Table 2. Variation of Specific Capacitance with Current Density of CT-$Co(OH)_2$ and CT-$Co(OH)_2$/Graphene Composite

current density	2 A/g (F/g)	6 A/g (F/g)	8 A/g (F/g)	10 A/g (F/g)
sp. cap. of CT-$Co(OH)_2$	285	218	188	161
sp. cap. of CT-$Co(OH)_2$/graphene	532	449	395	357

dx.doi.org/10.1021/sc400055z | ACS Sustainable Chem. Eng. 2013, 1, 1135−1142

prepared electroactive materials from the charge−discharge test were calculated by using the following equations

Energy Density

$$E = \frac{1}{2}C(\Delta V)^2 \quad (3)$$

Power Density

$$P = E/T \quad (4)$$

where C is the specific capacitance from the discharge curve, ΔV is the working potential, and T is the discharge time. The highest energy density of the CT-$Co(OH)_2$/graphene composite was calculated to be 36.20 Wh/kg at a power delivery rate of 700 W/kg. The high current response of the $Co(OH)_2$/graphene composite was also admirable with high energy density of 24.3 Wh/kg at a power density of 3500 W/kg. The maximum energy density for the CT-$Co(OH)_2$ was calculated to be 6.33Wh/kg at 400W/kg power density.

The EIS of all three electrode materials have been represented in terms of a Nyquist plot after fitting with an equivalent electrical circuit and is represented in Figure 8(a), and the electrical circuit

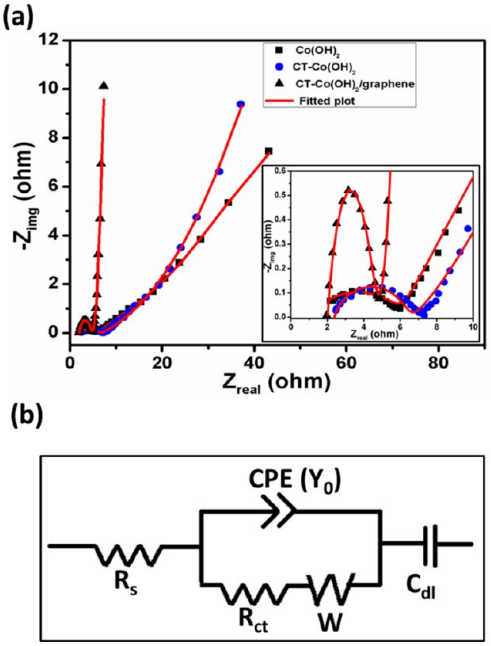

Figure 8. (a) Nyquist plots of $Co(OH)_2$, CT-$Co(OH)_2$, and CT-$Co(OH)_2$/graphene composite after fitting with an equivalent electrical circuit. (b) The equivalent circuit used for fitting the Nyquist plots.

is shown in Figure 8(b). EIS was performed within the frequency range of 0.1−1 MHz under an AC voltage amplitude of 5 mV. The equivalent electrical circuit consists of a resistive element (R_s) in a series combination with (CPE/(R_{ct} + W_d)) and a double-layer capacitor (C_{dl}). The resistive term R_s is a representative of bulk resistance, which is a combination of pore electrolyte resistance, bulk electrolyte resistance, and the contact resistance between the current collector and the electroactive material. In the Nyquist plot, R_s is represented as the real axis intercept of the impedance plot and was calculated to be 2.3, 2.2, and 2 ohm, respectively, for the $Co(OH)_2$, CT-$Co(OH)_2$, and CT-$Co(OH)_2$/graphene composite. All the Nyquist plots start with a flattened semicircle loop in the high frequency region followed by a linear part along an imaginary impedance axis. The initial semicircle is a characteristics of charge transfer resistance (R_{ct}), which was calculated to be 3.7, 3.9, and 2.7 ohm, respectively, for the $Co(OH)_2$, CT-$Co(OH)_2$, and CT-$Co(OH)_2$/graphene composite. The R_{ct} is a representative of the electrochemical reaction resistance, also known as faradaic resistance, and determines the rate of response of the electrode material in particular electrolyte.[30] The post-semicircle straight line in the low frequency region reflects the diffusion of the electroactive species, and the line with higher slope signifies lower diffusion resistance. The graphene-based hybrid composite of CT-$Co(OH)_2$, having a higher slope, indicates a more facile ion diffusion process through the electrode material. The highly conducting and mesoporous graphene ensure the utilization of the CT-$Co(OH)_2$/graphene material in terms of both lower charge transfer and lower ion diffusion resistance. The constant phase element is a nonintuitive circuit element to quantify the real world capacitor response and appears due to the edge effect and nonuniform distribution of reaction sites and current transfer at the electrode surface. The CPE constant (n) generally varies within the range of 0.5−1 for a supercapacitor. A higher CPE constant demonstrates better electrode performance and was evaluated as 0.88, 0.74, and 0.71, respectively, for the CT-$Co(OH)_2$/graphene composite, CT-$Co(OH)_2$, and $Co(OH)_2$ electrode. The double-layer capacitance was 1000 times higher for the CT-$Co(OH)_2$/graphene (91.87×10^{-3} F) compared to that of $Co(OH)_2$ (7.78×10^{-6} F) and CT-$Co(OH)_2$ (3.92×10^{-6} F). The high double-layer capacitance is attributed to the presence of high surface area graphene in the composite material.

CONCLUSION

In this work, we have hydrothermally prepared $Co(OH)_2$ with and without using CTAB. CTAB helps to develop hexagonal architecture in $Co(OH)_2$, which eventually increases the rate capability when used as an electrode material. The high utilization of the CTAB-controlled hexagonal architecture $Co(OH)_2$ as a pseudocapacitor was achieved in its graphene-based composite exhibiting a maximum specific capacitance of 532 F/g at a 2 A/g discharge current density accompanying a 94% specific capacitance retention over 500 consecutive charge−discharge cycles. The excellent cyclic stability of the $Co(OH)_2$/graphene composite combining a high energy density of 36.20 Wh/kg at a power delivery rate of 700 W/kg enables its excellent performance as an superior electrode material.

ASSOCIATED CONTENT

Supporting Information

Additional information regarding materials and instruments and characterizations. This material is available free of charge via the Internet at http://pubs.acs.org.

AUTHOR INFORMATION

Corresponding Author

*Tel.: +91-3222-283978. Fax: +91-3222-282700/255303. E-mail: chapal12@yahoo.co.in.

Notes

The authors declare no competing financial interest.

ACKNOWLEDGMENTS

The authors thank UGC INDIA for financial support and IIT Kharagpur for instrumental help.

REFERENCES

(1) Conway, B. *Electrochemical Supercapacitors*; Kluwer Academic/Plenum Publishers: New York, 2nd ed., 1999.

(2) Kötz, R.; Carlen, M. Principles and applications of electrochemical capacitors. *Electrochim. Acta* **2000**, *45*, 2483−2498.

(3) Ania, C. O.; Khomenko, V.; Raymundo-Pinero, E.; Parra, J. B.; Beguin, F. The large electrochemical capacitance of microporous doped carbon obtained by using a zeolite template. *Adv. Funct. Mater.* **2007**, *17*, 1828−1836.

(4) Xia, H.; Meng, Y. S.; Yuan, G.; Cui, C.; Lu, L. A symmetric RuO_2/RuO_2 supercapacitor operating at 1.6 V by using a neutral aqueous electrolyte. *Electrochem. Solid-State Lett.* **2012**, *15*, A60−A63.

(5) Yez, C.; Lin, Z. M.; Hui, S. Z. Electrochemical and capacitance properties of rod-shaped MnO_2 for supercapacitor. *J. Electrochem. Soc.* **2005**, *152*, A1272−A1278.

(6) Purushothaman, K. K.; Suba Priya, V.; Nagamuthu, S.; Vijayakumar, S.; Muralidharan, G. Synthesising of ZnO nanopetals for supercapacitor applications. *Micro Nano Lett.* **2011**, *6*, 668−670.

(7) Yu, Z.; Dai, Y.; Chen, W. Synthesis and characterization of nanoflakes β-$Ni(OH)_2$ microspheres for supercapacitors. *Adv. Mat. Res.* **2011**, *230−232*, 306−309.

(8) Jiang, H.; Ma, J.; Li, C. Hierarchical porous $NiCo_2O_4$ nanowires for high-rate supercapacitors. *Chem. Commun.* **2012**, *48*, 4465−4467.

(9) Cao, F.; Pan, G. X. P.; Tang, S.; Chen, H. F. Hydrothermal-synthesized $Co(OH)_2$ nanocone arrays for supercapacitor application. *J. Power Source* **2012**, *216*, 395−399.

(10) Simon, P.; Gogotsi, Y. Materials for electrochemical capacitors. *Nat. Mater.* **2008**, *7*, 845−854.

(11) Miller, J. R.; Simon, P. Electrochemical capacitors for energy management. *Science* **2008**, *321*, 651−652.

(12) Ji, X.; Hallam, P. M.; Houssein, S. M.; Kadara, R.; Lang, L.; Banks, C. E. Printable thin film supercapacitors utilizing single crystal cobalt hydroxide nanosheets. *RSC Adv.* **2011**, *2*, 1508−1515.

(13) Hu, Z.; Mo, L.; Feng, X.; Shi, J.; Wang, Y.; Xie, Y. Synthesis and electrochemical capacitance of sheet-like cobalt hydroxide. *Mater. Chem. Phys.* **2009**, *114*, 53−57.

(14) Yuan, C.; Zhang, X.; Gao, B.; Li, J. Synthesis and electrochemical capacitance of mesoporous $Co(OH)_2$. *Mater. Chem. Phys.* **2007**, *101*, 148−152.

(15) Yuan, C.; Yang, L.; Hou, L.; Li, D.; Shen, L.; Zhang, F.; Zhang, X. Synthesis and supercapacitance of flower-like $Co(OH)_2$ hierarchical superstructures self-assembled by mesoporous nanobelts. *J. Solid State Electrochem.* **2012**, *16*, 1519−1525.

(16) Li, J. T.; Zhao, W.; Huang, F. Q.; Manivannan, A.; Wu, N. Q. Single-crystalline $Ni(OH)_2$ and NiO nanoplatelet arrays as supercapacitor electrodes. *Nanoscale* **2011**, *3*, 5103−5109.

(17) Yu, G. H.; Hu, L. B.; Vosgueritchian, M.; Wang, H. L.; Xie, X.; McDonough, J. R.; et al. Solution-processed Graphene/MnO_2 nanostructured textiles for high-performance electrochemical capacitors. *Nano Lett* **2011**, *11*, 2905−2911.

(18) Yan, J.; Wei, T.; Qiao, W. M.; Shao, B.; Zhao, Q. K.; Zhang, L. J.; et al. Rapid microwave-assisted synthesis of graphene nanosheet/Co_3O_4 composite for supercapacitors. *Electrochim. Acta* **2010**, *55*, 6973−6978.

(19) Xi, Y.; Huang, X.; Lin, Z.; Zhong, X.; Huang, Y.; Duan, X. One-step strategy to graphene/$Ni(OH)_2$ composite hydrogels as advanced 3D supercapacitor electrode materials. *Nano Res.* **2103**, *6*, 65−76.

(20) Zhao, C.; Wang, X.; Wang, S.; Wang, Y.; Zhao, Y.; Zheng, W. Synthesis of $Co(OH)_2$/graphene/Ni foam nano-electrodes with excellent pseudocapacitive behavior and high cycling stability for supercapacitors. *Int. J. Hydrogen Energy* **2012**, *37*, 11846−11852.

(21) Qian, W.; Chen, Z.; Eastman, M.; Cottingham, S.; Manhat, B. A.; Goforth, A. M.; Jiao, J. Complementary microscopy techniques applied for optimizing the structure and performance of graphene-based hybrids. *Ultramicroscopy* **2012**, *119*, 97−101.

(22) Al-Ghoul, M.; El-Rassy, H.; Coradin, T.; Mokalled, T. Reaction−diffusion based co-synthesis of stable α- and β-cobalt hydroxide in bio-organic gels. *J. Cryst. Growth* **2010**, *312*, 856−862.

(23) Barmi, A-A. M.; Aghazadeh, M.; Arhami, B.; Shiri, H. M.; Fazl, A. A.; Jangju, E. Porous cobalt hydroxide nanosheets with excellent supercapacitive behavior. *Chem. Phys. Lett.* **2012**, *541*, 65−69.

(24) Tang, S. C.; Vongehr, S.; Wang, Y.; Chen, L.; Meng, X. K. Ethanol-assisted hydrothermal synthesis and electrochemical properties of coral-like β-$Co(OH)_2$ nanostructures. *J. Solid State Chem.* **2010**, *183*, 2166−2173.

(25) Zhu, L. P.; Zhang, W. D.; Xiao, H. M.; Yang, Y.; Fu, S. Y. Facile synthesis of metallic Co hierarchical nanostructured microspheres by a simple solvothermal process. *J. Phys. Chem. C.* **2008**, *112*, 10073.

(26) Wang, L. Z.; Zhang, J. L.; Chen, F.; Anpo, M. Fluoride-induced reduction of CTAB template amount for the formation of MCM-48 mesoporous molecular sieve. *J. Phys. Chem. C.* **2007**, *111*, 13648.

(27) Liu, Z.; Ma, R.; Osada, M.; Takada, K.; Sasaki, T. Selective and controlled synthesis of α- and β-cobalt hydroxides in highly developed hexagonal platelets. *J. Am. Chem. Soc.* **2005**, *127*, 13869−13874.

(28) El-Enany, G. M.; Ghanem, M. A.; Abd El-Ghaffar, M. A. Electrochemical deposition and characterization of poly(3,4-ethylene dioxythiophene), poly(aniline) and their copolymer onto glassy carbon electrodes for potential use in ascorbic acid oxidation. *Port. Electrochim. Acta.* **2010**, *28*, 336.

(29) Qi, Z. Y.; Hui, X. X.; Jing, K.; Ping, TU. J. Hydrothermal synthesized porous $Co(OH)_2$ nanoflake film for supercapacitor application. *Chin. Sci. Bull.* **2012**, *57*, 4215−4219.

(30) Qiao, Y.; Li, C. L.; Bao, S.-J.; Bao, Q.-L. Carbon nanotube/polyaniline composite as anode material for microbial fuel cells. *J. Power Sources.* **2007**, *170*, 79−84.